**ISCI, Volume *3***

## Supplemental Information

# Mesoporous $TiO_2$/TiC@C Composite Membranes with Stable $TiO_2$-C Interface for Robust Lithium Storage

**Wei Zhang, Lianhai Zu, Biao Kong, Bingjie Chen, Haili He, Kun Lan, Yang Liu, Jinhu Yang, and Dongyuan Zhao**

**Supplemental Data Items**

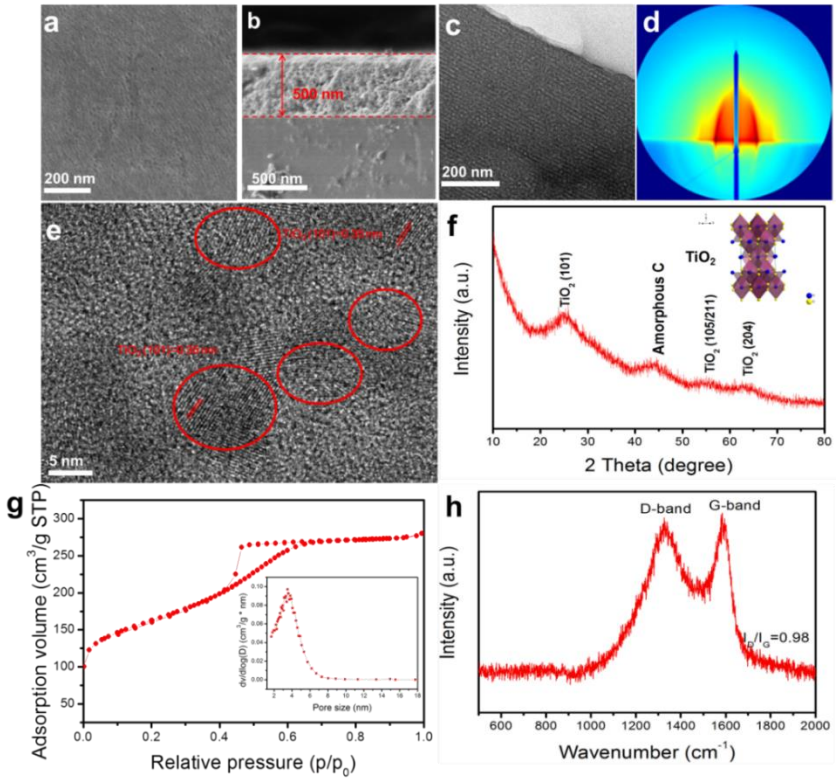


**Figure S1. Structure and composition characterizations of the mesoporous $TiO_2$@C membranes, related to Figure 2.**

Top-view SEM image (a), cross-section SEM image (b), low-magnification TEM image (c), GISAXS image (d), high-resolution TEM (HRTEM) image (e), XRD pattern (f), BET analysis (g), and Raman spectrum (h) of the mesoporous $TiO_2$@C membranes. The inset in (f) shows the molecule structure of $TiO_2$. The inset in (g) is pore size distribution.

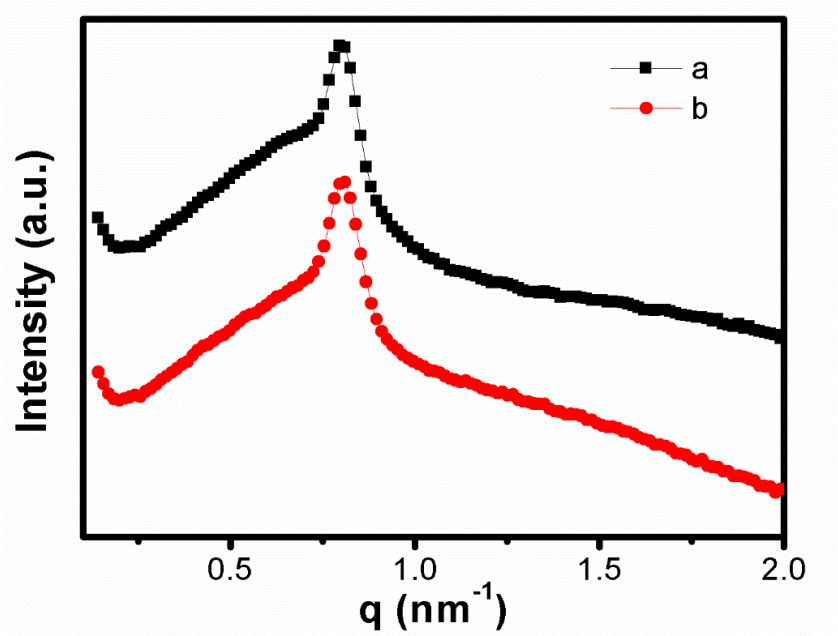


**Figure S2. Small angel X-ray diffraction (SAXS), related to Figure 2**

SAXS patterns of the mesoporous $TiO_2$@C (a) and $TiO_2$/TiC@C (b) membranes.

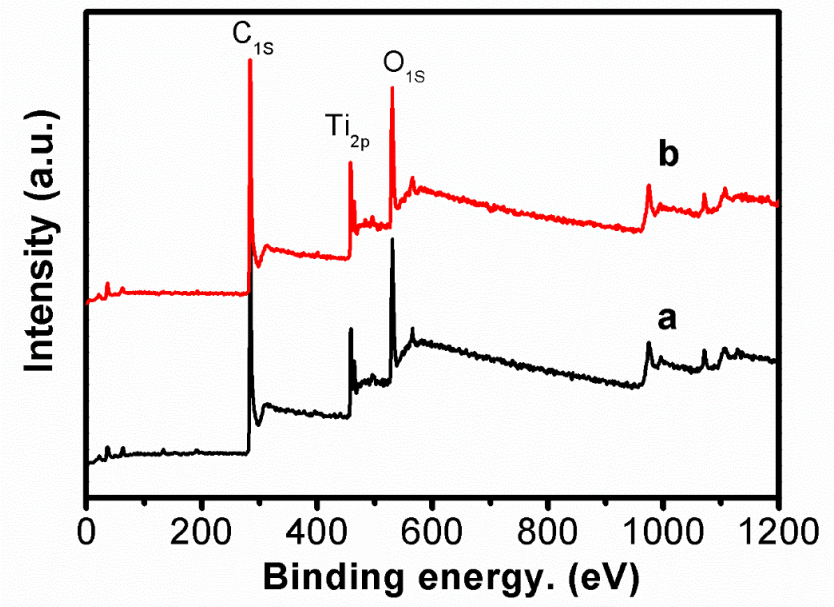


**Figure S3. X-ray photoelectron spectroscopy (XPS), related to Figure 2.**
XPS spectra of the mesoporous $TiO_2$@C (a) and $TiO_2$/TiC@C (b) membranes.

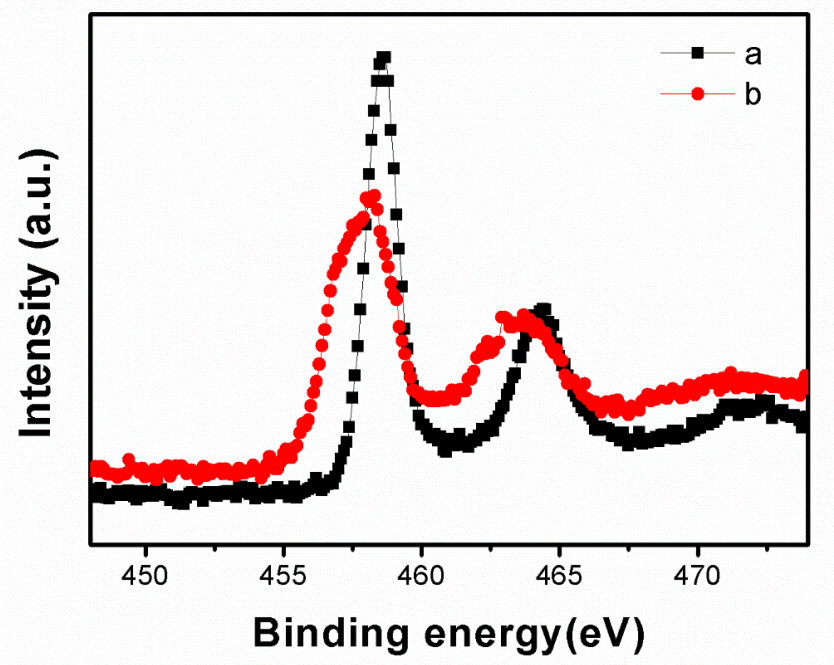


**Figure S4. High-resolution XPS spectra, related to Figure 2.**
High-resolution XPS spectra of Ti 2p core level for the $TiO_2$@C (a) and $TiO_2$/TiC@C (b) membranes.

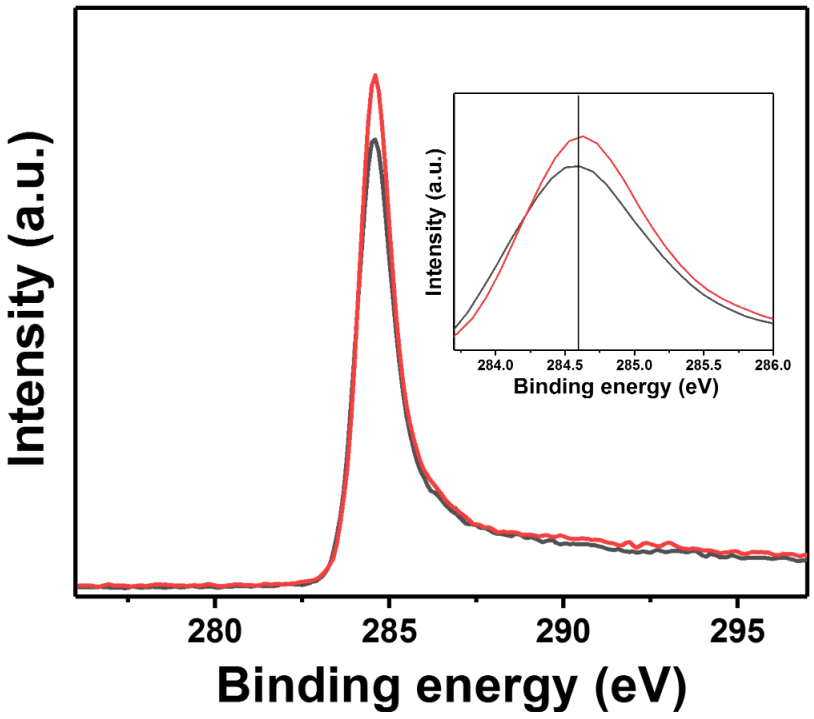


**Figure S5. High-resolution XPS spectra, related to Figure 2.**

High-resolution XPS spectra of C1s core level for the $TiO_2$@C (a) and $TiO_2$/TiC@C (b) membranes.

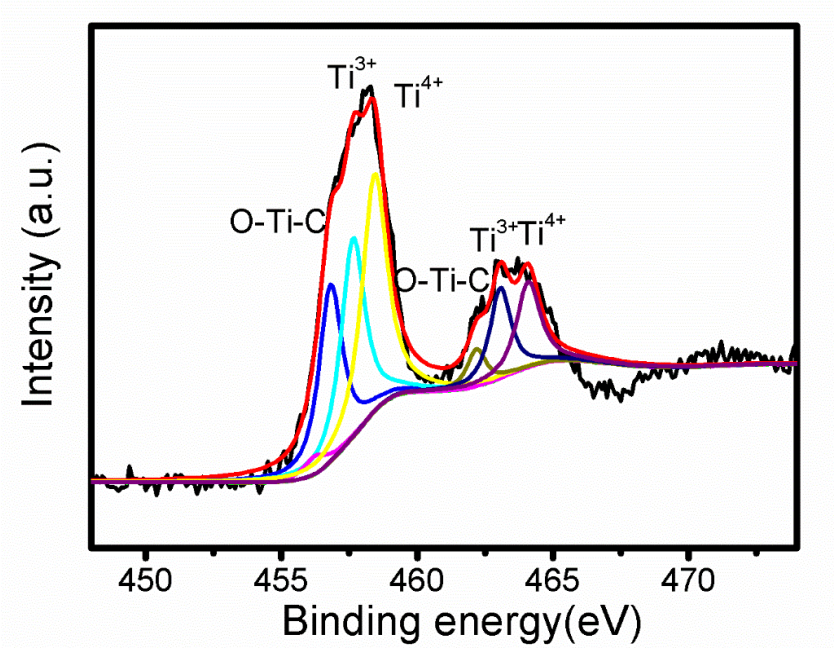


**Figure S6. High-resolution XPS spectra, related to Figure 2.**

The high-resolution XPS spectrums of Ti 2p core level for the mesoporous $TiO_2$/TiC@C membranes. The HRXPS contained six components at 456.8, 457.7, 458.5, 462.2, 463.1 and 464.2 eV are consistent with O-Ti-C, $Ti^{3+}$, $Ti^{4+}$, O-Ti-C, $Ti^{3+}$, and $Ti^{4+}$, respectively.

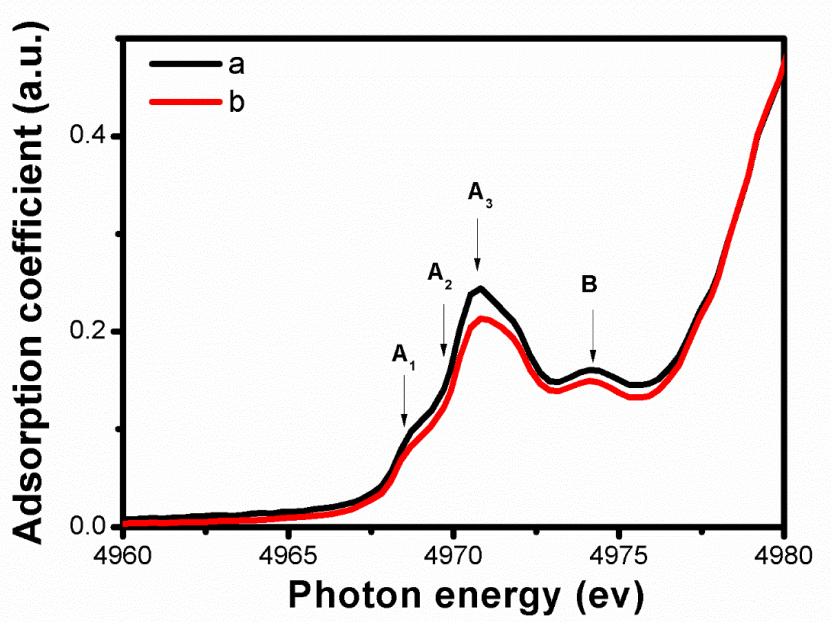


**Figure S7. X-ray absorption fine structure spectroscopy (XAFS), related to Figure 2.**

The Ti K-edge pre-edge XAFS of the mesoporous $TiO_2$@C (a) and $TiO_2$/TiC@C (b) membranes.

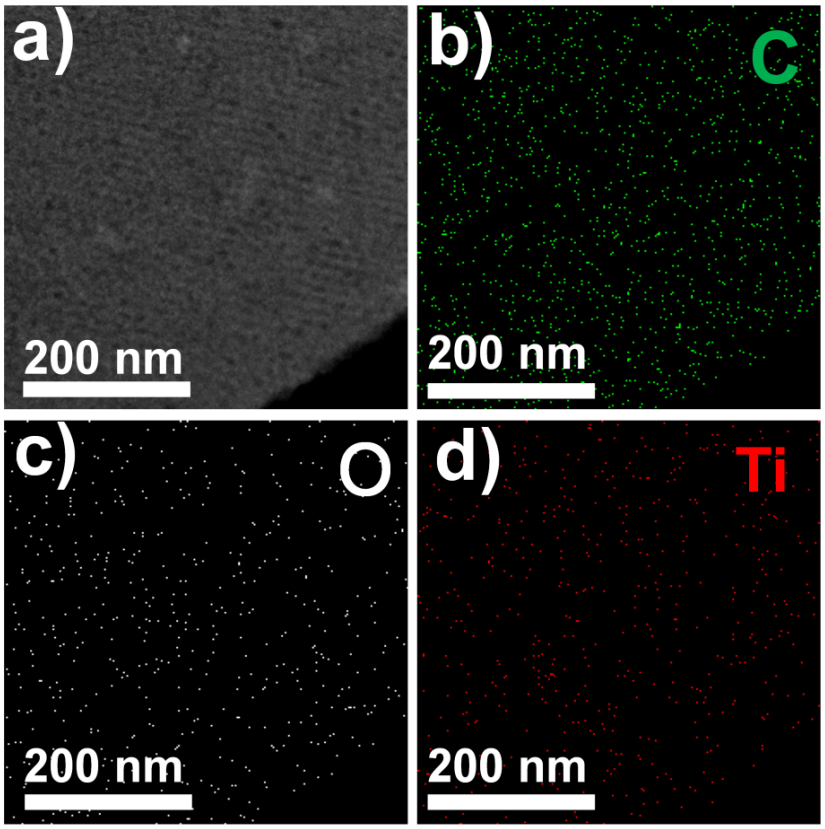


**Figure S8. Elemental mapping, related to Figure 2.**

The elemental mapping of the mesoporous $TiO_2$@C membranes. HAADF-STEM (a) image and energy-dispersive X-ray element mapping of C (b), O (c), and Ti (d) elements.

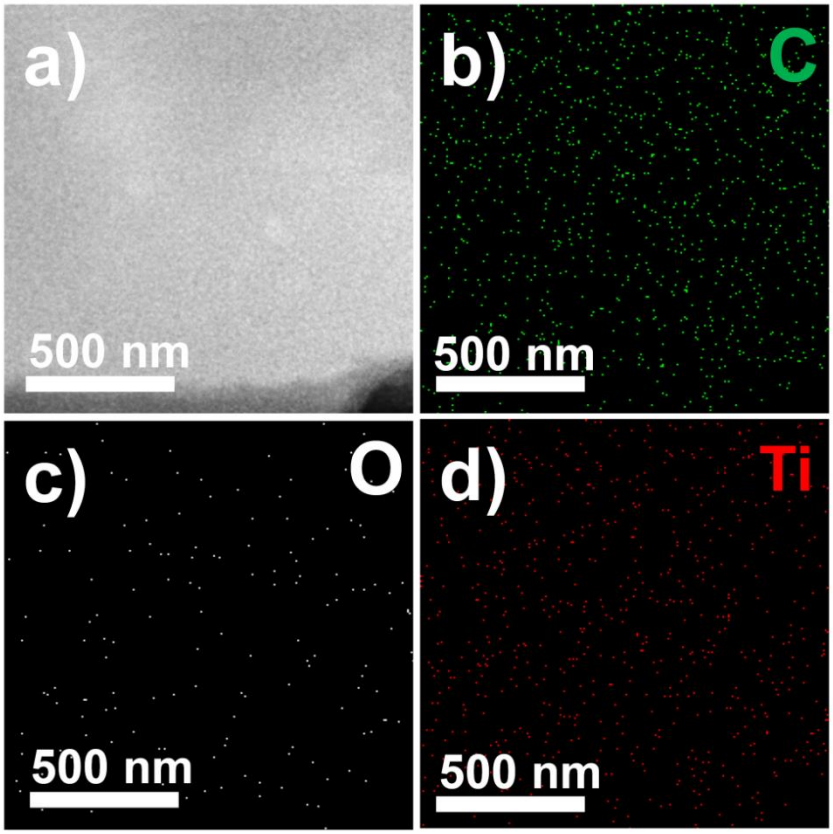


**Figure S9. Elemental mapping, related to Figure 2.**

The elemental mapping of the mesoporous $TiO_2$/TiC@C membranes. HAADF-STEM (a) image and energy-dispersive X-ray element mapping of C (b), O (c), and Ti (d) elements.

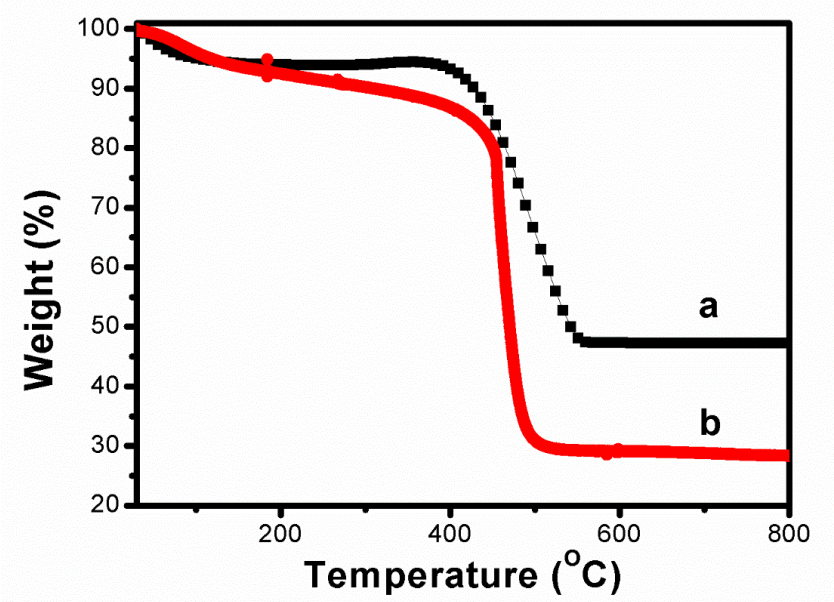


**Figure S10.Thermogravimetric analysis, related to Figure 2.**

The thermogravimetric analysis curves of the mesoporous $TiO_2$/TiC@C membranes before (a) and after (b) the removal of $TiO_2$ nanocrystals by concentrated sulfuric acid.

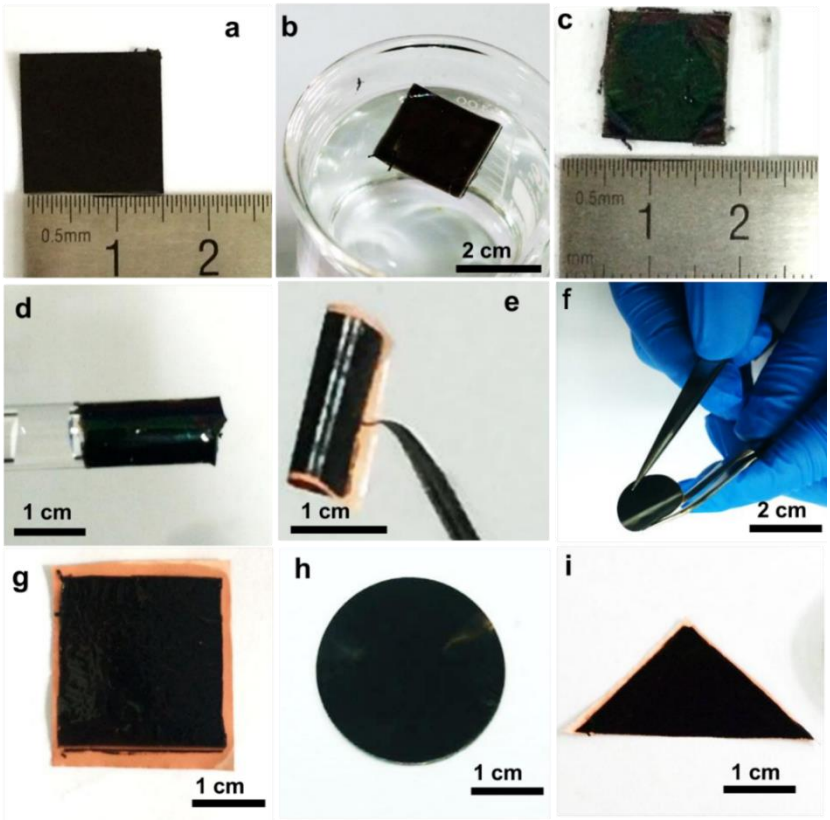


**Figure S11**. **Transferability, flexibility, tailorability of the mesoporous membranes, related to Figure 2.**

Photographs of the mesoporous $TiO_2$/TiC@C membranes formed on silicon wafer (a), floating on water (b), transferred onto glass substrate (c), transferred onto a cylindrical substrate (d), bent without cracks (e, d), and tailored to different shapes (g, h, i).

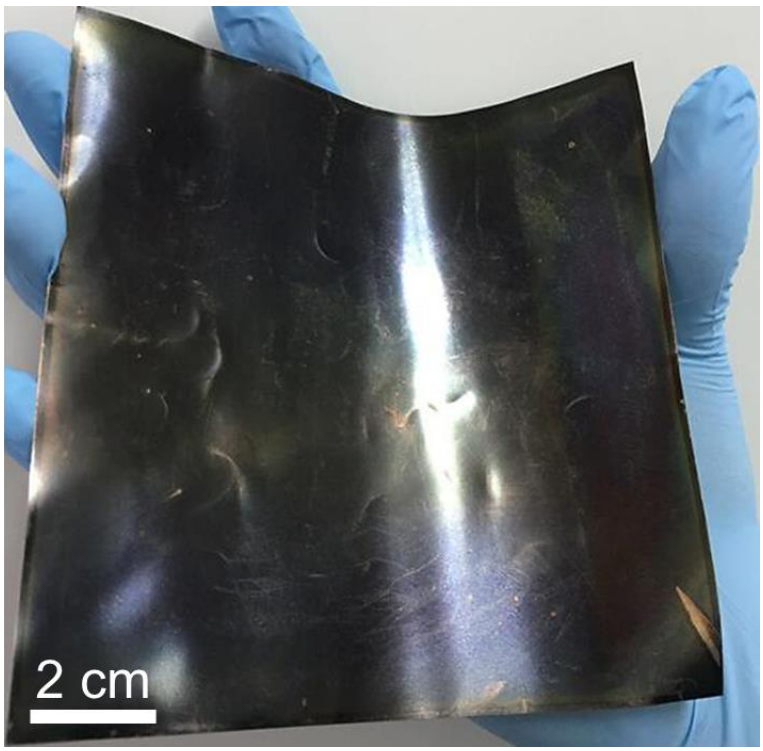


**Figure S12**. **Processing scalability of the mesoporous membranes, related to Figure 2.**

Photograph of the mesoporous $TiO_2$/TiC@C membranes formed on a large Ti foil of 144 $cm^2$.

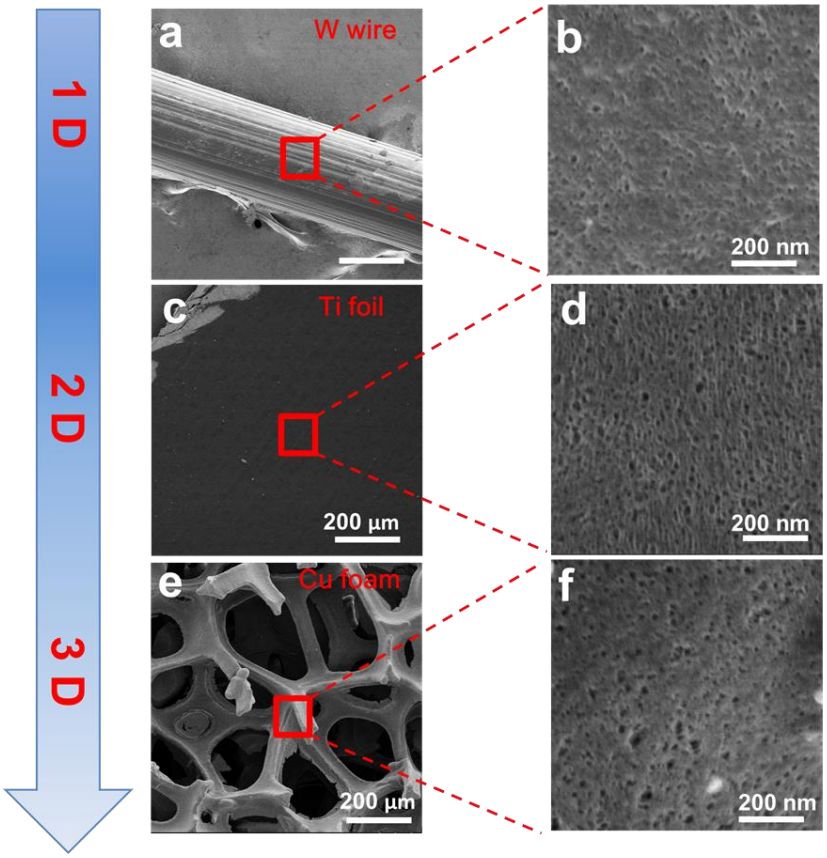


**Figure S13. Processing feasibility of the mesoporous membranes, related to Figure 2.**

SEM images of mesoporous $TiO_2$/TiC@C membranes formed on different substrates. (a,b) W wires, (c,d) Ti foils and (e,f) Cu foams.

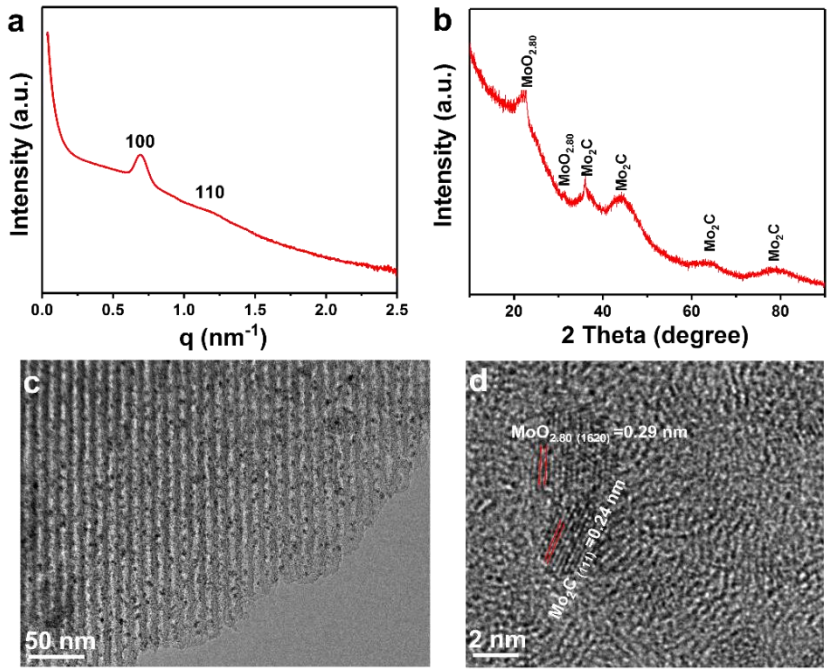


**Figure S14. Extension of the synthetic strategy, related to Figure 2.**
SAXS (a), XRD (b), TEM (c) and HRTEM (d) images of mesoporous $MoO_{2.80}/Mo_2C$@C composites.

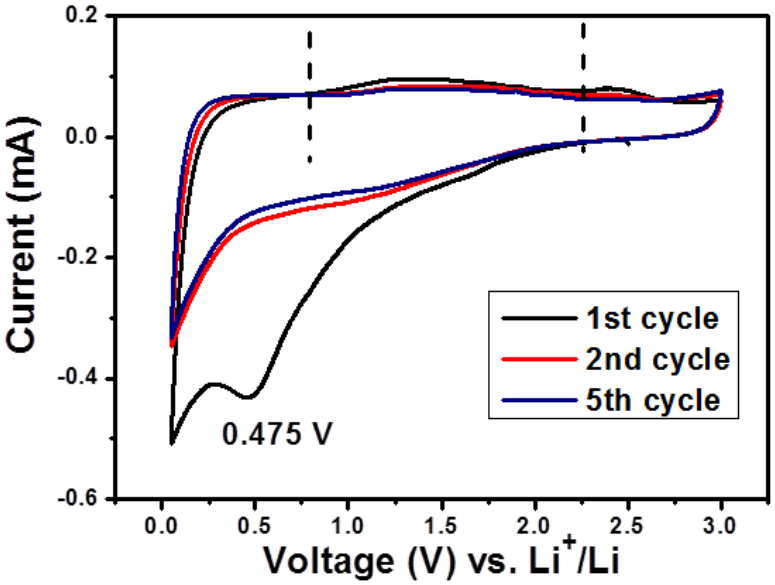


**Figure S15. Electrochemical performance of the mesoporous $TiO_2$@C membranes, related to Figure 3.**

Cyclic voltammograms of the mesoporous $TiO_2$@C membranes electrodes in a voltage range of 0.01–3 V at a scanning rate of 1 $mV \cdot s^{-1}$.

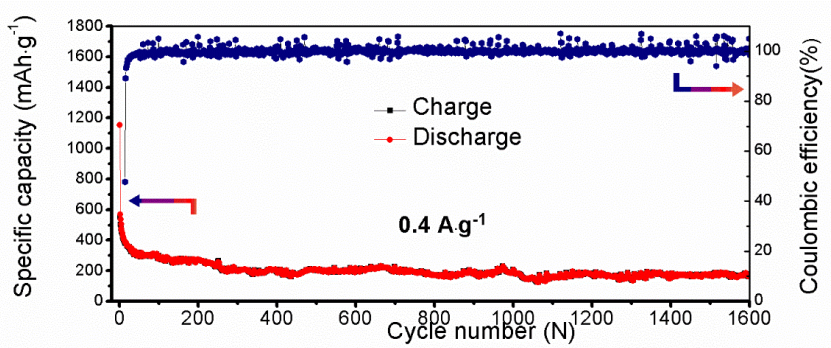


**Figure S16**. **Electrochemical performance of the mesoporous $TiO_2$@C membranes, related to Figure 3.**

Cycling performances of the mesoporous $TiO_2$@C membranes at a current density of 0.4 $A \cdot g^{-1}$.

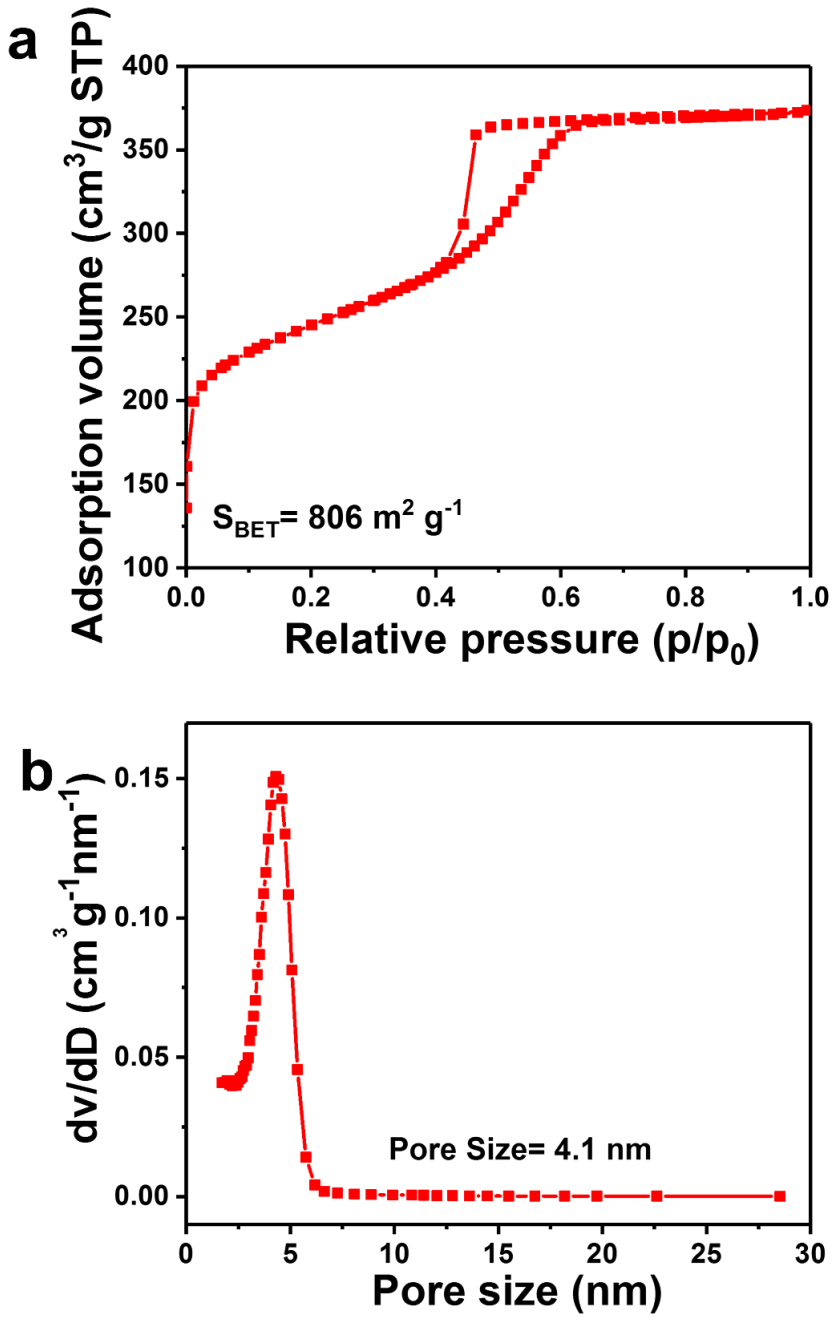


**Figure S17. Structure characterizations of the mesoporous carbon, related to Figure 3.**

$N_2$ adsorption-desorption isotherms (a) and the corresponding pore size distribution (b) of the mesoporous carbon annealed at 900 °C.

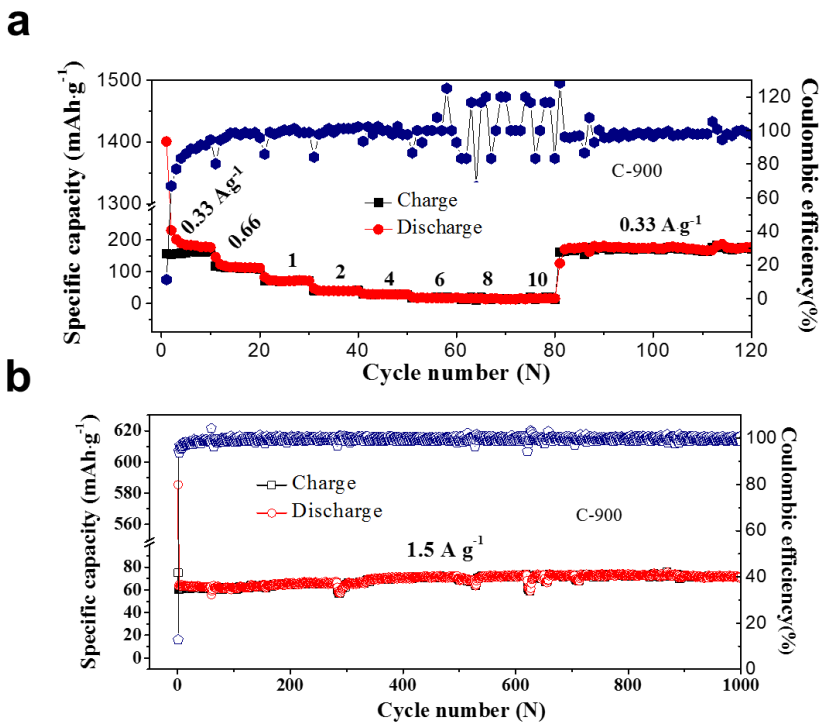


**Figure S18. Electrochemical performances of the mesoporous carbon, related to Figure 3.**

(a) Rate performance of mesoporous carbon annealed at 900 °C. (b) Cycling performance of mesoporous carbon annealed at 900 °C.

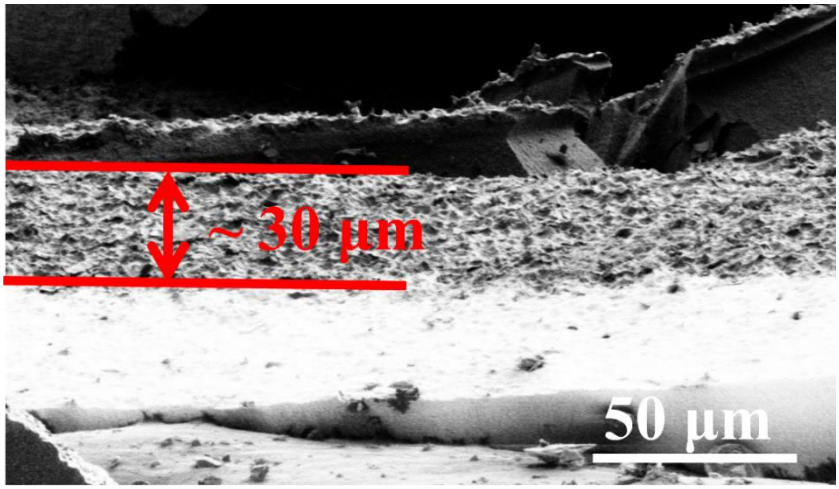


**Figure S19. Structure characterizations of the thicker mesoporous $TiO_2$/TiC@C membrane, related to Figure 3.**

Cross-section SEM image of the mesoporous $TiO_2$/TiC@C membranes with a thickness of ~30 µm synthesized at 100 rpm for 5 s.

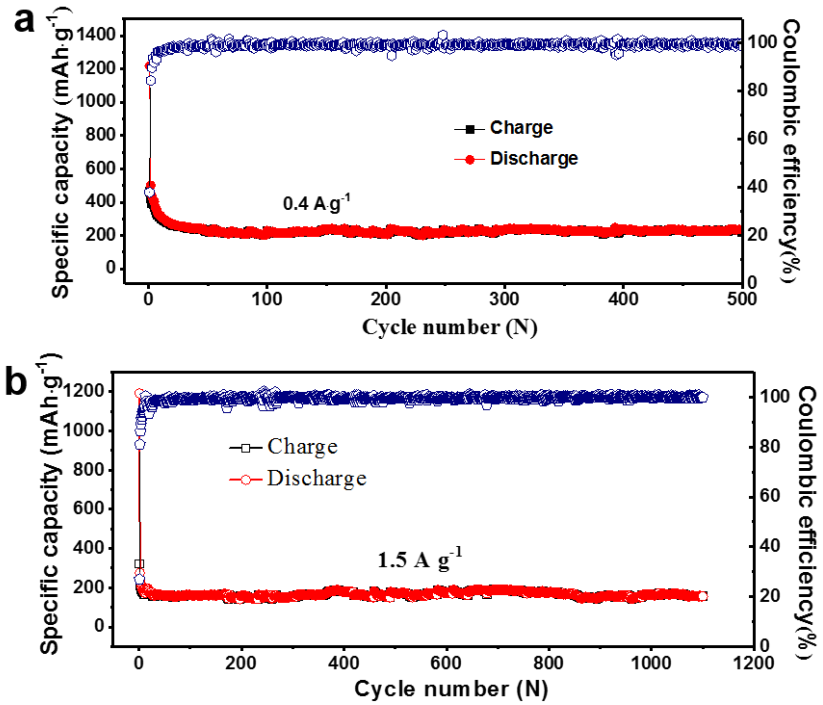


**Figure S20. Electrochemical performances of the thicker mesoprous $TiO_2$/TiC@C membranes, related to Figure 3.**

Cycling performance of the mesoporous $TiO_2$/TiC@C membranes with a thickness of ~ 30 μm at current densities of 0.4 (a) and 1.5 $A \cdot g^{-1}$ (b), respectively.

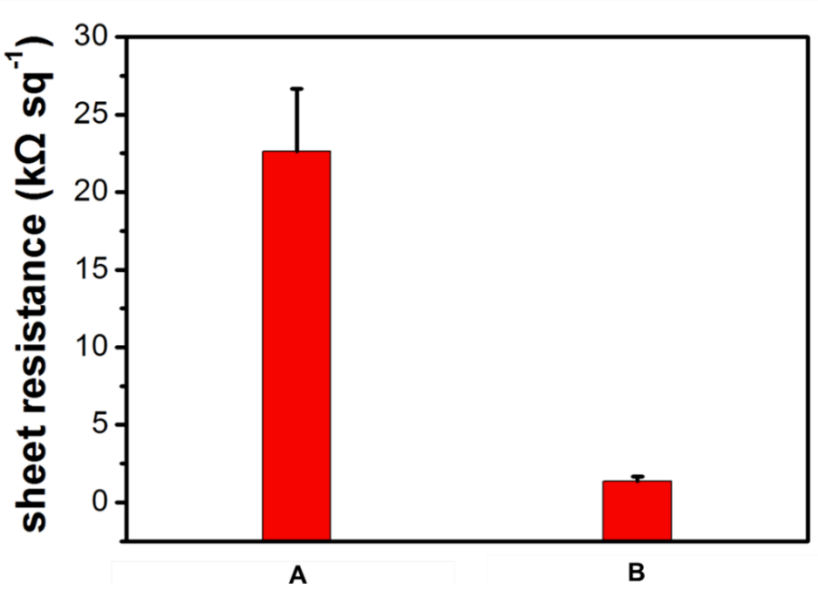


**Figure S21**. **Sheet resistances, related to Figure 3.**

The sheet resistances of the mesoporous $TiO_2$@C (A) and $TiO_2$/TiC@C (B) membranes.

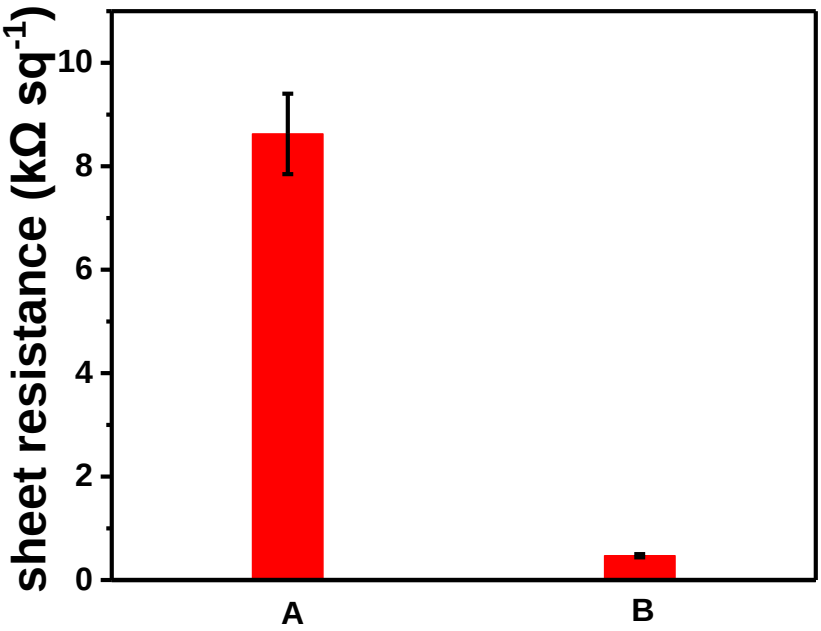


**Figure S22**. **Sheet resistances, related to Figure 3.**
The sheet resistances of the mesoporous carbon membranes calcination at 700 (A) and 900 °C (B), respectively.

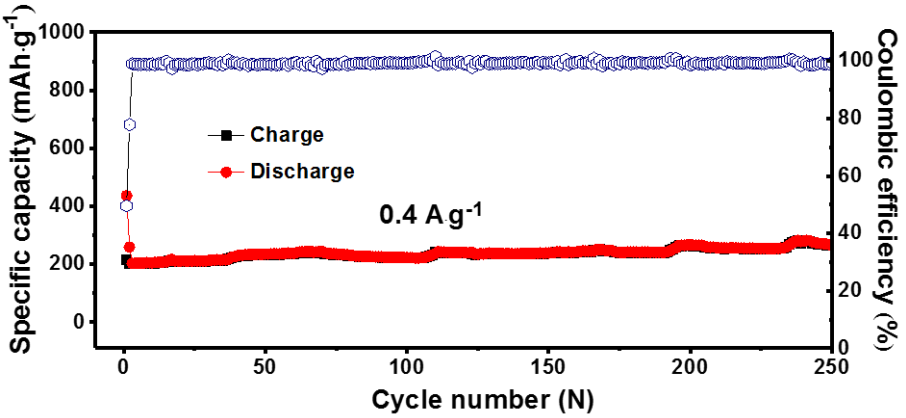


**Figure S23. Electrochemical performance of the mesoporous $TiO_2$/TiC@C membrane after prelithiation, related to Figure 3.**

Cycling performance of the mesoporous $TiO_2$/TiC@C membranes electrodes at current densities of 0.4 $A \cdot g^{-1}$ after prelithiation. The initial coulomb efficiency is increasing from 35.3 to 49.6% after prelithiation.

**Figure S24**. **Flexible full battery, related to Figure 3.**
Photograph of the flexible full battery assembled by using the $TiO_2$/TiC@C membranes as the anode (Cu foil as the current collector) and commercial $LiCoO_2$ loaded on Al foil as the cathode.

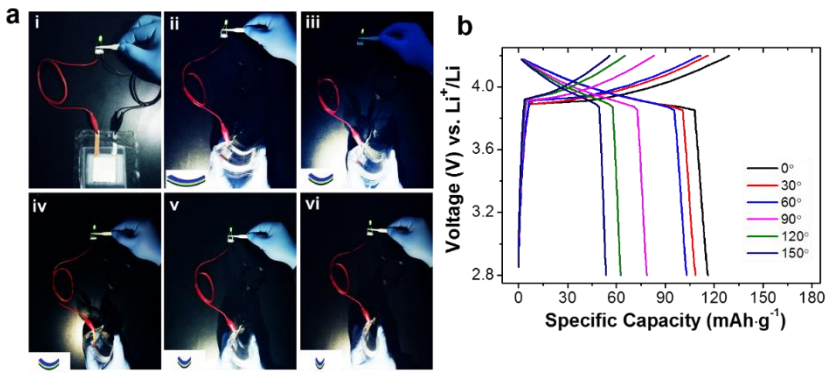


**Figure S25. Electrochemical performance of the flexible full battery, related to Figure 3.**

(a) Photographs of the flexible full battery with different bent angels and a LED can be stably lit. The bent angle is measured to be 0 (i), 30 (ii), 60 (iii), 90 (iv), 120 (v) and 150°(vi), respectively. (b) Charge/discharge curves of the flexible full battery with different bent.

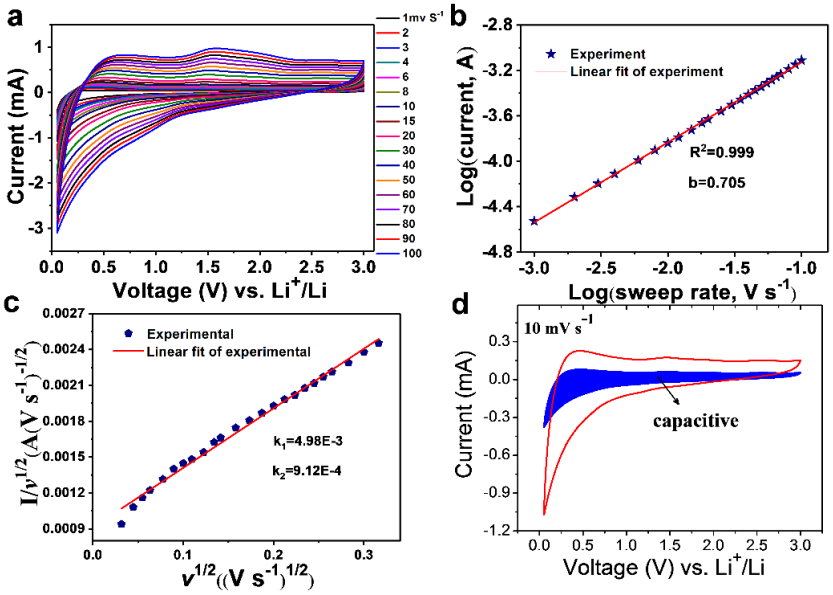


**Figure S26. Electrochemical kinetics analysis of the mesoporous carbon, related to Figure 4.**

(a) CV curves at various scan rates from 2 to 200 mV $s^{-1}$ of the mesoporous carbon membranes. (b) Log(*i*) vs. log (*v*) plots of the cathodic current response at ~ 2.05 V of the mesoporous carbon membrane electrodes. (c). I/scan $rate^{1/2}$ versus scan $rate^{1/2}$. (d) Separation of the capacitive and diffusion currents in the mesoporous carbon membrane electrodes at a scan rate of 10 mV $s^{-1}$.

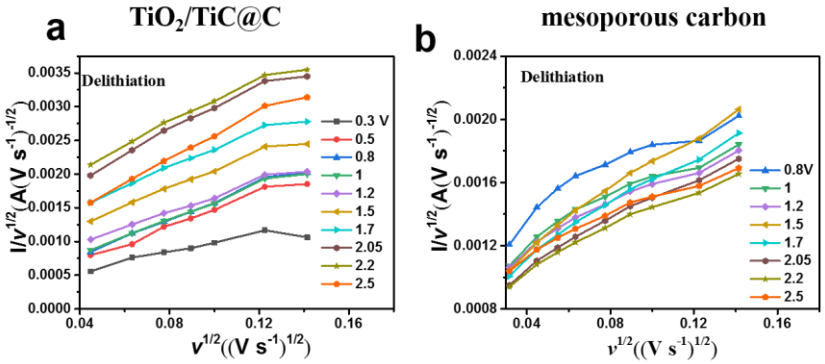


**Figure S27. Electrochemical kinetics analysis of the mesoporous carbon and $TiO_2$/TiC@C c membranes, related to Figure 4.**

CV curves of (a) mesoporous carbon, (b) $TiO_2$/TiC@C membranes at different scan rates, and corresponding plots of $\nu^{1/2}$ vs. $i/\nu^{1/2}$ used for calculating constants $k_1$ and $k_2$ at different potentials.

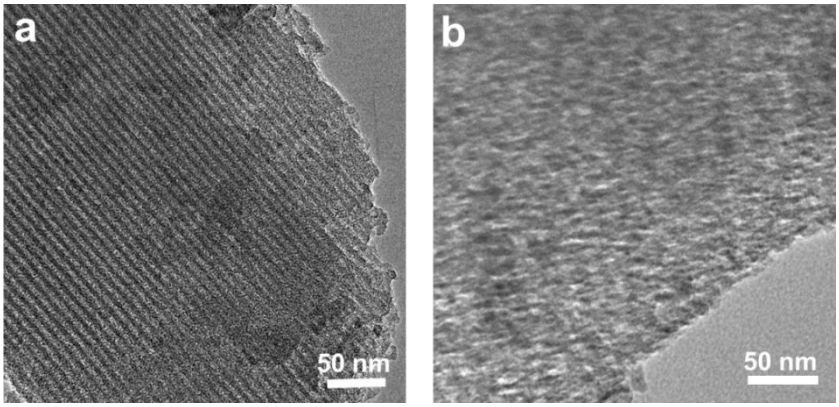


**Figure S28**. **Structural evolution of the mesoporous carbon, related to Figure 5.** TEM images of the mesoporous carbon before (a) and after (b) 1000 cycles at the current density of 0.4 $A \cdot g^{-1}$.

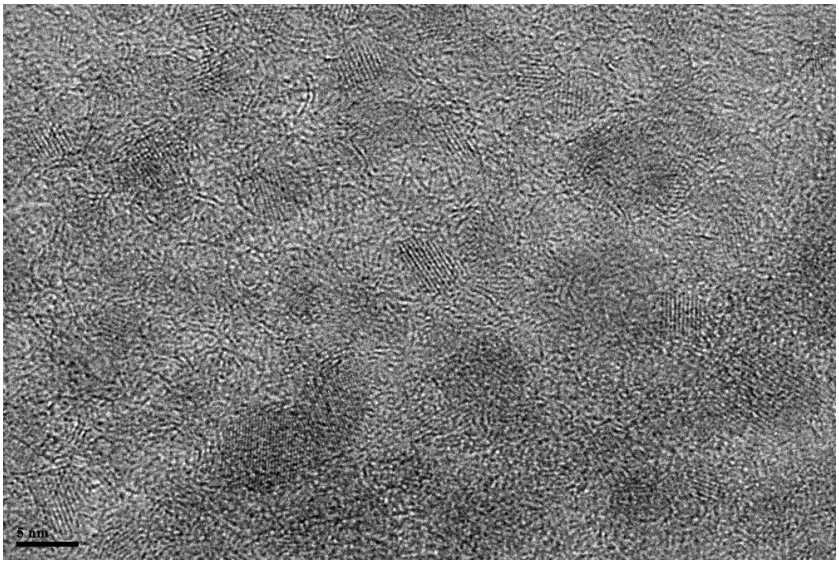


**Figure S29. Structural evolution of the mesoporous $TiO_2$/TiC@C membranes, related to Figure 5.**

HRTEM image of the mesoporous $TiO_2$/TiC@C membranes after 1,600 cycles at the current density of 0.4 $A \cdot g^{-1}$.

**Table S1. Structural and textural properties of the mesoporous $TiO_2$@C and $TiO_2$/TiC@C membranes, related to Figure 2.**

| | $S_{BET}$ ($m^2/g$) | $S_{Micro}$ ($m^2/g$) | $V$ ($cm^3/g$) | $Dp$ (nm) |
|---|---|---|---|---|
| *$TiO_2$/C* | 501 | 147 | 0.38 | 4.02 |
| *$TiO_2$/TiC@C* | 674 | 276 | 0.42 | 3.78 |

**Table S2. A summary for the cycling performance of the ordered mesoporous $TiO_2$/C and $TiO_2$@TiC/C membranes, related Figure 3.**

| | *Current density ($A\ g^{-1}$)* | *Capacity** | | *Capacity retention (%)* | *Coulombic efficiency (%)* | *Cycle number* |
|---|---|---|---|---|---|---|
| | | *Gravimetric capacity ($mAh \cdot g^{-1}$)* | *Volumetric capacity ($mAh \cdot cm^2$)* | | | |
| *$TiO_2$/TiC@C* | 0.4 | 244 | 705 | 85.1 | 99.3 | $1600^{th}$ |
| | 1.5 | 150 | 434 | 68.4 | 99.4 | $5000^{th}$ |
| *$TiO_2$/C* | 0.4 | 161 | 465 | 38.7 | 99.7 | $1600^{th}$ |

*The results summarized from Figure 3c in the manuscript and Figure S16 in the supporting information. The capacities are calculated by active materials.

**Table S3. Rate performance comparison between the $TiO_2$/TiC@C composite and mesoporous carbon，related Figure 3.**

| *Current density (A $g^{-1}$)* | *Capacity ($mAg^{-1}$)* | | *Capacity ratio* |
|---|---|---|---|
| | *$TiO_2$/TiC@C (TTC)* | *mesoporous carbon (MC)* | *MC/TTC* |
| 0.33 | 278 | 163 | 0.58 |
| 0.66 | 250 | 107 | 0.43 |
| 1 | 179 | 71 | 0.4 |
| 2 | 138 | 40 | 0.29 |
| 4 | 105 | 28 | 0.27 |
| 6 | 80 | 17 | 0.21 |
| 8 | 60 | 16 | 0.27 |
| 10 | 56 | 13 | 0.24 |
| 0.33 | 280 | 170 | 0.61 |

*The result summarized from Figure 3b in the manuscript and Figure S19 in the supporting information.

## Transparent Methods

### Materials Synthesis

**Preparation of resol precursors**: The phenolic resol precursors were prepared according to the previous report (Zhao et al., 2005). In a typical synthesis, 8.0 g of phenol was melted in a flask at 45 °C and then mixed with 1.68 g of NaOH solution (20 wt %) under stirring. After 10 min, 13.76 g of formalin (37 wt % formaldehyde) was added dropwise. Upon further stirring for 1 h at 70 °C , the mixture was cooled down to room temperature. The pH value was adjusted to ~7.0 by using 2.0 M HCl solution. Then the water was removed under vacuum at 49 °C . Finally, ethanol was added to precipitate NaCl and dissolve the resol to obtain a 20 wt % solution.

**Preparation of titanium citrate complex**: The preparation procedure for titanium citrate complex was similar to the previous report (Waterland et al., 2004). For a typical preparation, 28.4 g (100 mmol) of titanium isopropoxiede was dissolved in 50 mL of ethanol (solution A) and 21.0 g (100 mmol) of citric acid was dissolved in 100 mL of ethanol (solution B). Solution B was dropped into the solution A under stirring at 40 °C for 2 h. Ethanol was then removed by rotary evaporation at 40 °C then white powders were obtained. Water was added to dissolve the white powders to obtain 1.0 M homogeneous solution.

The mesoporous $TiO_2$@C and $TiO_2$/TiC@C composite membranes were synthesized *via* a universal strategy by using the phenolic resol (see Supplemental Experimental Procedures for details), pluronic F127 and the titanium citrate complex (see Supplemental Experimental Procedures for details) as a carbon precursor, template and titanium precursor, respectively. The silicon wafers were first treated with piranha solution (98% sulfuric acid:30% hydrogen peroxide = 2:1 v/v) at 90 °C for 30 min to form a thin silica oxide layer on the surface as substrates. In a typical synthesis, 1.5 g of F127, 2.5 g of the resol and 3.0 g of the titanium citrate solution were dissolved in 16 mL of water/ethanol mixture (1:1 v/v). After stirring for 30 min at room temperature, the solution was coated onto the pretreated silicon wafer (2 cm × 2 cm) at 600 rpm for 10 s to form a thin film. The film was dried at 40 °C for 3–5 h, followed by aging at 100 °C for another 24 h. The mesoporous $TiO_2$@C and $TiO_2$/TiC@C composite membranes on the silicon wafer were obtained after pyrolyzing at 700 and 900 °C for 2 h in nitrogen, respectively. The ramping rate was 1 °C $min^{-1}$ below 600 °C, and 5 °C $min^{-1}$ above 600 °C. To obtain free standing membranes, a polymethyl methactylate (PMMA) solution was spin-coated onto the composite membranes to increase the toughness. Afterward, the obtained membranes supported by PMMA thin films were immersed into a potassium hydroxide solution (10 wt %) at room temperature for 8–10 h to etch the silica layer on the surface of silicon wafer. After the PMMA film was dissolved by anisole, the free-standing membranes with a size of 2 cm × 2 cm were obtained.

### Electrochemical Measurements

The electrochemical performances of the membrane electrodes were evaluated in 2016-type coin cells. The cells were set up by using the mesoporous $TiO_2$/TiC@C composite membranes standing on copper foils as work electrodes and commercial lithium disks as the counter electrodes, respectively. A non-aqueous solution of 1.0 M $LiPF_6$ in a 1:1:1

of ethylene carbonate (EC), diethyl carbonate (DEC), and dimethyl carbonate (DMC) was used as the electrolyte. For a flexible full cell, the commercial $LiCoO_2$ coating on aluminum foil was used as the counter electrode. The electrode was dried at 80 °C over night at a vacuum oven before assembly. All the cells were assembled in a glove box with $[O_2]$, $[H_2O] \leq 1$ ppm. Specific capacities were calculated based on the weight of membranes (~ 5 μm, ~0.5 mg). The galvanostatic charge/discharge test was conducted on LAND cycler (Wuhan LAND electronics Co., China) under ambient temperature. Cyclic voltammetry measurements were carried out at a scan rate of 1 $mV \cdot s^{-1}$ under the voltage range of 0.01 ~ 3 V by using a CHI 660e electrochemical workstation (Chen-Hua Instruments Co., China). Electrochemical impedance spectra were recorded using the Solatron 1260/1287 Electrochemical Interface (Solatron Metrology, UK) with oscillation amplitude of 5 mV at the frequency range from 100 mHz to 100 kHz.

**Full Battery Assembly**

To assemble a flexible full battery, a 30 × 30 $mm^2$ $TiO_2$/TiC@C anode was coupled with a $LiCoO_2$ cathode, which was prepared by coating conventional $LiCoO_2$ nanoparticle slurry on an Al foil (mass loading: ~ 3.0 mg $cm^{-2}$). Prior to the assembly, the $TiO_2$/TiC@C anode was prelithiated by placing it in direct contact with a wet Li foil and the electrolyte for 12 h to compensate its large initial irreversible capacity. The mass ratio of the $TiO_2$/TiC@C and $LiCoO_2$ in the full battery was adopted as 1:2, considering the difference in specific capacity of the two electrodes. The specific capacity is calculated based on the $LiCoO_2$ mass because the battery is cathode-limited. The battery was packaged with a flexible polyethylene foil bag by edge bonding machine, and the same electrolyte as used in the coin cells was injected when placed inside an argon-filled glovebox. The full batteries were cycled in the range of 2.8 – 4.2 V on LAND galvanostatic charge/discharge instruments.

**Material Characterization**

X-ray diffraction (XRD) patterns were collected by a Bruker D8 powder X-ray diffractometer (Germany) with Cu Kα radiation (40 kV, 40 mA). Small-angle X-ray scattering (SAXS) patterns were recorded by a Nanostar U small-angle scattering system (Bruker, Germany) with Cu Kα radiation (40 kV, 35 mA). GISAXS measurements were carried out at beamline BL16B1 of Shanghai Synchrotron Radiation Facility (SSRF). The incident X-ray photon energy was 10 keV and a MAR165 area detector was used to record the scattering intensity. The *d*-spacing values were calculated using the formula $d = 2\pi/q$, where $q=4\pi (\sin\theta)/\lambda$. Field emission scanning electron microscopy (FESEM) images were obtained on a Hitachi S4800 field-emission SEM (Japan) operated at 1 kV and 10 μA. Transmission electron microscope (TEM) measurements were conducted on a JEOL 2100F microscope (Japan) at 200 kV. For TEM measurements, the samples were prepared by sonication in ethanol and suspended on holey carbon grids. $N_2$ adsorption-desorption isotherms were measured with a Micromeritics Tristar 2420 analyzer at 77 K. Before measurements, the samples were degassed at 180 °C for more than 5 h. The Brunauer-Emmett-Teller (BET) method was utilized to calculate the specific surface areas. The pore size distributions were derived from the desorption branches of the isotherms based on Barrett-Joyner-Halenda (BJH) model. The total pore volumes were estimated from the

amount adsorbed at a relative pressure ($P/P_0$) of 0.995. Thermogravimetric analysis (TGA) curves were carried out using a Mettler Toledo TGA-SDTA851 analyzer (Switzerland) from 30 to 800 °C in an air flow of 80 mL $min^{-1}$ at a heating rate of 10 °C $min^{-1}$.

**Supplemental References:**


Meng, Y., Gu, D., Zhang, F., Shi, Y., Yang, H., Li, Z., and Zhao, D. (2005). Ordered mesoporous polymers and homologous carbon frameworks: amphiphilic surfactant templating and direct transformation. Angew. Chem. Int. Ed. 44, 7053-7059.

Kemmitt, T., Al-Salim, N.I., Gainsford, G.J., Bubendorfer, A. and Waterland, M. (2004). Unprecedented oxo-titanium citrate complex precipitated from aqueous citrate solutions, exhibiting a novel bilayered $Ti_8O_{10}$ structural core. Inorg. Chem. 43, 6300-6306.